Nanoscale Res Lett (2009) 4:1421–1427
DOI 10.1007/s11671-009-9414-7

NANO EXPRESS

Persistent Photoconductivity Studies in Nanostructured ZnO UV Sensors

Shiva Hullavarad · Nilima Hullavarad · David Look · Bruce Claflin

Received: 8 April 2009 / Accepted: 7 August 2009 / Published online: 28 August 2009

Abstract The phenomenon of persistent photoconductivity is elusive and has not been addressed to an extent to attract attention both in micro and nanoscale devices due to unavailability of clear material systems and device configurations capable of providing comprehensive information. In this work, we have employed a nanostructured (nanowire diameter 30–65 nm and 5 μm in length) ZnO-based metal–semiconductor–metal photoconductor device in order to study the origin of persistent photoconductivity. The current–voltage measurements were carried with and without UV illumination under different oxygen levels. The photoresponse measurements indicated a persistent conductivity trend for depleted oxygen conditions. The persistent conductivity phenomenon is explained on the theoretical model that proposes the change of a neutral anion vacancy to a charged state.

Keywords Persistent photoconductivity · Semiconducting II–VI materials · Zinc oxide · UV sensor · Nanoscale device

Introduction

The synthesis methods and the use of nanostructures for various applications have been a very lucrative topic in the last decade [1]. These efforts have lead to discoveries of unknown phenomena and/or new approaches to explain with precision the observed experimental and theoretical facts from the macro/micro world [2]. When all is said and done, the issues in nano-sized devices (individual or arrays) and basic impediments in device operation have not been addressed largely due to not having a perception of end-user requirements, leaving the device's operational bottlenecks unaddressed [3]. This is true for two well-researched opto-electronic materials GaN- [4] and ZnO-based [5] devices like light-emitting diodes and photodetectors. In the case of GaN, more emphasis was given to high crystal quality growth, epitaxy, and understanding the Mg–H complex in determining the p-doping that eventually lead a lone scientist, S. Nakamura at Nichia Chemical Industries, Japan, to invent the first working solid state blue laser. In case of ZnO, the large part of the investment from university and industry arenas is still devoted to realizing the p-type doping along with some initial success from M. Kawasaki's group at Tohoku University, Japan that recently demonstrated the first ZnO p–n homojunction light-emitting diode [6].

ZnO is emerging as a potential candidate due to its direct wide bandgap and its ability to tailor electronic, magnetic, and optical properties through doping and alloying. One significant property that has brought ZnO and its alloys with Mg to the forefront of a flurry of research activity is the large exciton binding energy (60 meV when compared to 25 meV for GaN) for use in UV lasers. ZnO has been widely reported as a visible-blind UV sensor [7] over a wide range of applications in military and non-military arenas [8] that includes missile plume detection for hostile missile tracking, flame sensors, UV source monitoring, and calibration. However, recent research in nanostructures of ZnO has proved that the reduced dimensions have the potential to provide more

S. Hullavarad (✉) · N. Hullavarad
Office of Electronic Miniaturization, University of Alaska, Fairbanks, AK 99701, USA
e-mail: shiva.h@alaska.edu

D. Look · B. Claflin
Semiconductor Research Center, Wright State University, Dayton, OH 45435, USA

untapped properties if harnessed in a systematic manner. Many simple fabrication techniques [9], devices [10, 11], and applications [12] have been demonstrated and reproduced. ZnO nanoscale structures such as one-dimensional nanowires are attracting more attention because of their enormous potential as fundamental building blocks for nanoscale electronic [13] and photonic devices due to the enhanced sensitivity offered by quantum confinement effects [14]. In this work, we address the prominent defect-related property (could be sum or individual defects due to non-crystallinity, surface charge imbalance, or substrate to film interface strains) that affects the electrical properties of the ensuing device. The phenomenon of persistent photoconductivity (PPC) is a situation in which a photo-induced current in the device continues to flow even after the exciting photon source is turned off. PPC is a major issue in device operation that became a topic of intense research interest during development of GaN [15, 16] and AlGaN [17] photodetectors. The motivation of the present work is to understand the origin of PPC in ZnO by employing a simple device configuration consisting of a metal–semiconductor–metal structure. PPC is very difficult to observe in bulk materials and needs to be measured at very low temperature, which in turn complicates the carrier transport mechanisms, thus limiting the ability to extract and interpret the exact cause of the problem [18]. This phenomenon is observable in both macro and nanostructured films; however, the effects are more prominent in nanostructured materials due to singularity in their joint density of states, thus allowing a bulk phenomenon to be observable clearly even at room temperature.

Experimental

ZnO nanowires were synthesized in a horizontal tube furnace that was programmed for a processing temperature of 800 °C with heating rate 10 °C min^{-1}. The source material Zn (99.9%) in granular form was placed at the center of the furnace. Double side-polished Al_2O_3 (0001) and Si (100) samples were used as substrates for optical characterization. In the initial stage, the furnace was flushed by Ar gas and was stabilized. When the furnace reached 420 °C, the Zn metal evaporated and O_2 gas was introduced with a combined Ar/O_2 gas mixture. The evaporated Zn metal formed ZnO nanostructures when the reactants achieved supersaturation and was deposited on substrates and also on the walls of the tube furnace. The process was carried out for 90 min and samples were removed after the furnace was cooled down to room temperature. ZnO nanostructures were characterized by environmental scanning electron microscope (E-SEM) (Electro Scan) and photo-luminescence (PL) at room temperature (Laser Science, Inc, Model VSL-337 ND-S, 337 nm, 6 mW and Ocean Optics SD5000 spectrometer) measurements to monitor the morphology and the bandgap. The X-ray photoelectron spectroscopy (XPS) measurements were performed using Kratos Axis 165 spectrometer at a vacuum of 4×10^{-10} Torr with non-monochromatic Mg $K\alpha$ radiation. All binding energies were calibrated with respect to C 1s at 284.6 eV.

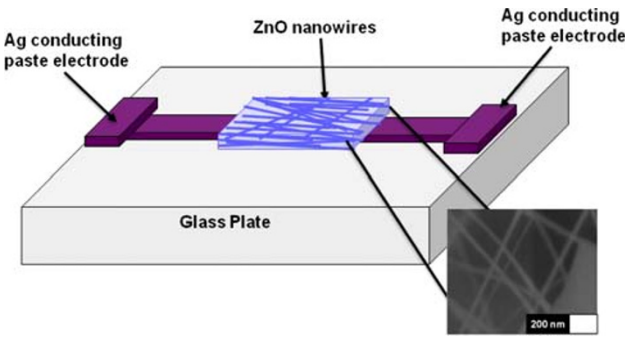

Fig. 1 Schematic of nanostructure ZnO sensor device

Sensors were fabricated on a glass plate with linear silver electrodes of dimension 0.1 cm × 2 cm with a gap of 80 μm as seen in the schematic, Fig. 1. ZnO nanostructures were dissolved in methanol and then applied to an area between the electrodes. The photoresponse measurements were carried out using a Xe arc lamp, a Thermo Oriel monochromator setup, and lock-in-amplifier measurement setup. The experimental setup was calibrated with standard SiC and AlGaN UV sensors, and the output power of the Xe arc lamp was measured by a Newport standard power meter. To study the effect of oxygen on the photoresponse properties of the ZnO nanostructure UV sensors, the measurements were carried out in situ in a vacuum chamber at different oxygen pressure levels.

Results and Discussion

Figure 2 shows a SEM image of the as-grown ZnO nanowires in the form of a network on Al_2O_3 substrate. The ZnO nanowires are of uniform diameter, length, and density. The dimensions of the nanowires are approximately 30–65 nm in diameter and about 5 μm in length. Figure 3 shows the X-Ray Diffraction pattern of ZnO nanowires grown on Si (100) substrate. The pattern clearly depicts distinct peaks at 31.6°, 34.49°, and 36.27° corresponding to (100), (002) and (101) reflections [19]. The high intensity peak at 34.49° corresponding to the (002) reflection indicates that the ZnO nanowires are highly c-axis oriented and crystalline in nature. The XPS results for Zn2p and O1s for ZnO nanowire films are shown in Fig. 4. Chemical states and the presence of any possible compositions were analyzed after deconvoluting the spectra. The films show well

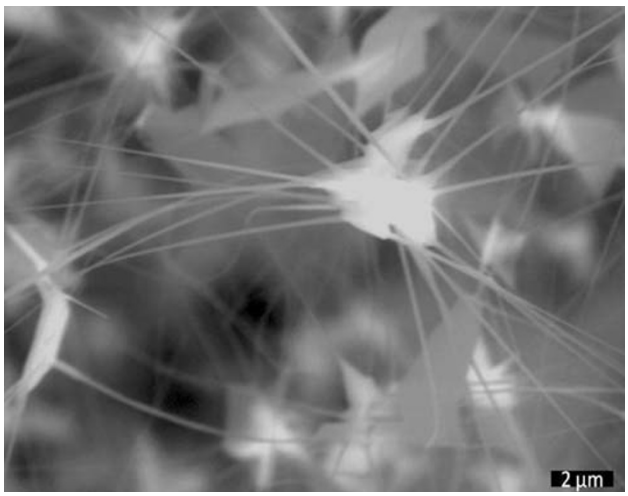

Fig. 2 SEM of ZnO nanowires on Al_2O_3 substrate

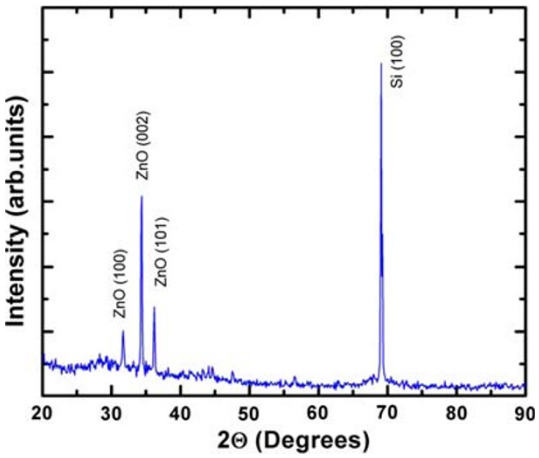

Fig. 3 X-ray diffraction pattern of ZnO nanowires grown on Si (100) substrate

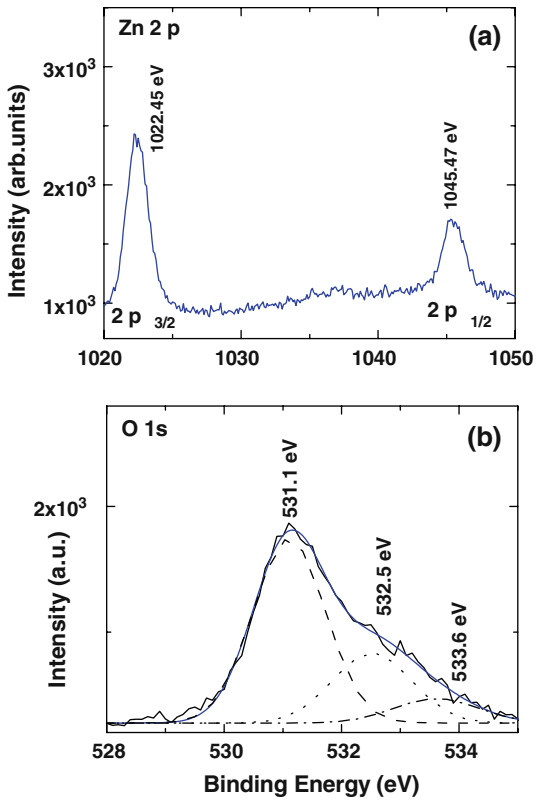

Fig. 4 XPS spectra of ZnO nanostructures **a** Zn 2p 3/2 and 1/2, **b** O1s core levels

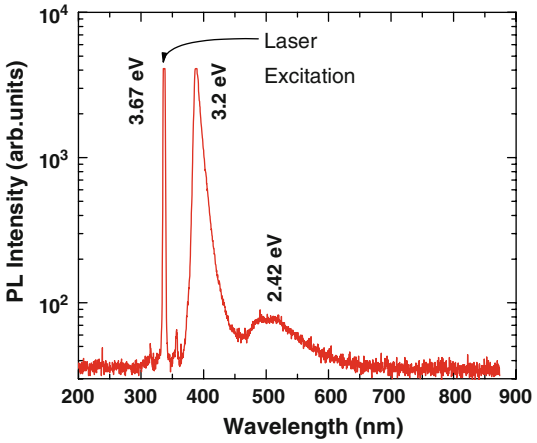

Fig. 5 PL spectrum of ZnO nanowires on Al_2O_3 substrate. The exciton peak is at 386 nm and the defect peak is at 510 nm. Laser excitation is at 3.67 eV

resolved peaks, Fig. 4a, at 1,022.45 and 1,045.47 eV corresponding to the doublet of Zn2p 3/2 and 1/2, respectively, as reported for ZnO [20]. Figure 4b shows the O1s spectrum in ZnO nanowire film. This asymmetric peak is resolved into three components at 531.1, 532.5, and 533.6 eV. The intense peak at 531.1 eV can be attributed to ZnO oxygen, whereas the shoulder peaks at 532.5 and 533.6 eV have been assigned to the chemisorbed oxygen. The relative concentration of Zn/O is calculated to be close to 1 from the photoelectron cross-sections and kinematic factors indicating the near perfect stoichiometry achieved in the present synthesis method. Figure 5 shows the PL spectrum of ZnO nanowires with a main peak at 386 and at 510 nm under laser excitation of 3.6 eV. The dominant peak at 386 nm is attributed to the recombination of free excitons corresponding to 3.2 eV (386 nm), wide direct bandgap transition of ZnO nanowires at room temperature [21]. The exciton peak has the sharp full width at half maximum (FWHM) width of 10 nm. The narrow width of the dominant emission is expected in the nanowires as a consequence of better quantum efficiency. The green emission at $\lambda = 510$ nm (2.42 eV) corresponds to deep levels because of the transition between the photo-excited holes and singly ionized oxygen vacancies. The weak green

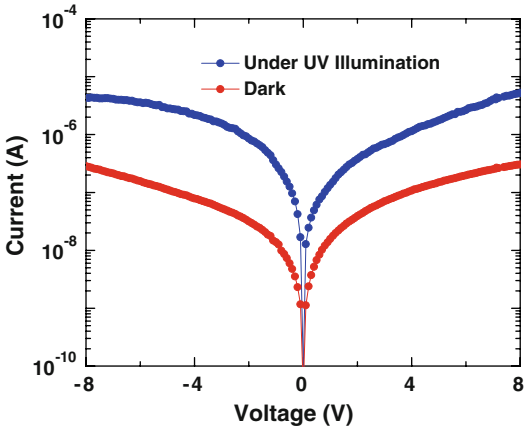

Fig. 6 Current–voltage characteristics of nanostructure ZnO photoconductor at room conditions with and without UV corresponding to the bandgap of ZnO

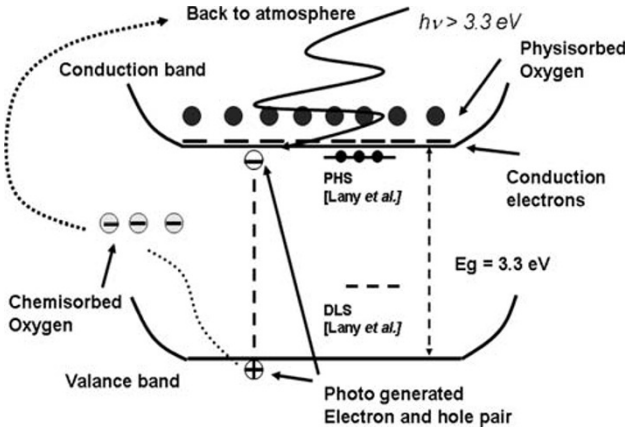

Fig. 7 Schematic of photoconduction in ZnO due to the desorption of chemisorbed oxygen. The deep localized state (DLS) and the perturbed host states (PHS) as suggested by Lany et al. are also shown

band emission (510 nm) indicates the lower concentration of defects [22].

The current–voltage characteristics with and without UV illumination (that corresponds to the bandgap of ZnO as observed in PL measurements in room conditions) are shown in Fig. 6. The dark (without illumination) current of the nanostructure ZnO UV sensor was 6×10^{-10} A at 1 V. The nanostructure ZnO UV sensor exhibited a photocurrent of 7×10^{-8} A, at 1 V under UV illumination (386 nm) at room temperature and pressure conditions. The UV to Visible rejection ratio was found to be two orders of magnitude. The lower dark current is a clear manifestation of reduced intrinsic defects as well as interfaces and trap states generated during the processing of the material and the device [23]. On the other hand, the UV sensors fabricated from conventional physical vapor deposition methods exhibited huge dark currents in the 10^{-3} A range [24]. The lower dark current observed in the present ZnO nanostructure devices indicates the better crystalline quality of the material. ZnO homojunctions formed between the p-type (Sb-doped ZnO hole concentration: 1×10^{16} cm^{-3}, mobility: 10 cm^2 V^{-1} S^{-1}, and resistivity: 6 Ω cm) and n-type ZnO (Ga-doped electron concentration: 1×10^{18} cm^{-3}, mobility: 6 cm^2 V^{-1} S^{-1}, and resistivity: 0.9 Ω cm) exhibited large dark current in the order of 0.4 mA at 1 V due to the presence of a large number of growth-related defects between the film and the substrate [24]. The large magnitude of dark current density indicates that there are considerable defects and dislocations in the ZnO film grown on a Si substrate, which is a typical result of heteroepitaxy between largely mismatched materials [25].

When a ZnO surface is exposed to oxygen, oxygen is adsorbed onto its surface. Each adsorbed oxygen ties up an electron from the conduction band creating a space charge layer (Fig. 7). This reduces the number of electrons available for conduction near the surface, contributing to a lower dark current. This effect is more prominent in nanostructures because of the near crystalline properties, as opposed to bulk films that tend to grow with enough grain boundaries, which trap/retrap the oxygen as a function of temperature giving rise to instability in measuring the dark current. When a photon of energy equal to or higher than the bandgap is incident on the ZnO surface, an electron–hole pair is generated. The positively charged hole neutralizes the chemisorbed oxygen, thereby releasing the electron back to the conduction band increasing the conductivity of the sample [26].

It has been reported in the literature [27] that the oxygen pressure surrounding the ZnO nanostructures significantly affects the photoconductivity. As the oxygen concentration varies, the width of the depletion region caused by the chemisorbed oxygen also varies, thereby creating a channel that widens or contracts. In order to verify this hypothesis, we carried out photoresponse measurements in controlled oxygen atmosphere in a vacuum chamber fitted with an optical port through which light (250–900 nm) can be incident on the nano ZnO sensor as seen in the schematic (Fig. 8). The vacuum chamber is fitted with a gas inlet manifold to control O_2 gas pressure during the photoresponse measurements. First, the chamber was evacuated to 1×10^{-5} Torr, sufficiently below the measurement pressure of 8×10^{-2} Torr. The pressure inside the chamber was increased to 8×10^{-2} Torr by letting in high purity oxygen gas into the chamber through the other inlet valve. The oxygen pressure of 8×10^{-2} Torr was maintained throughout the photoresponse measurements. After this set of measurements, O_2 gas pressure inside the chamber was increased to 4×10^{-1} Torr, and photoresponse studies were carried out. Finally, the oxygen pressure inside the chamber was raised to 7.6×10^2 Torr and held constant throughout the photoresponse measurements.

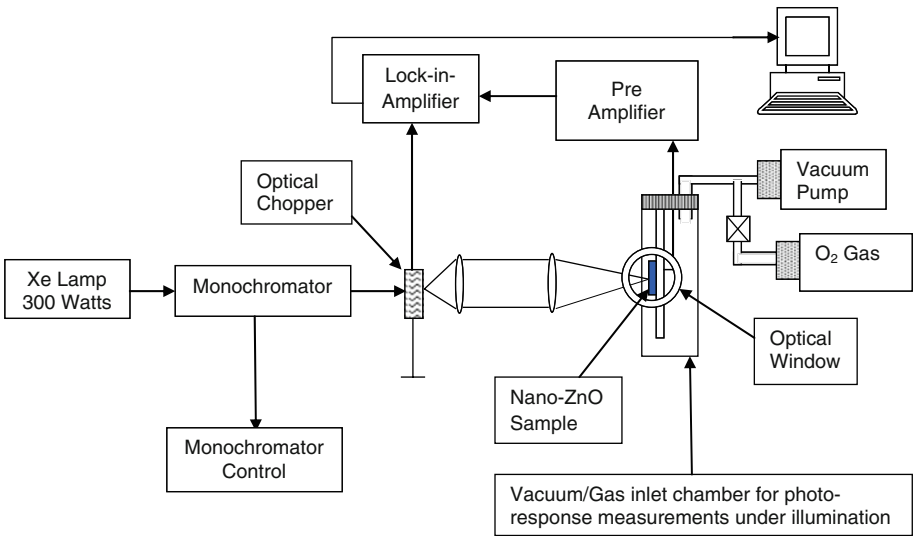

Fig. 8 Schematic of photoresponse measurements setup, a vacuum chamber fitted with an optical port through which light (250–900 nm) can be incident on the nano ZnO sensor

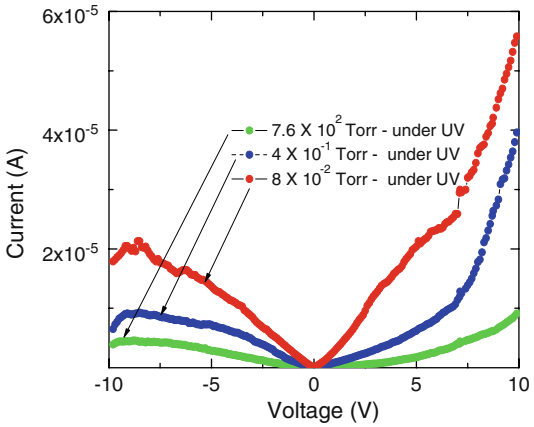

Fig. 9 Current–Voltage characteristics of nanostructure ZnO UV sensor for O_2 pressures of 7.6×10^2, 4×10^{-2}, and 8×10^{-2} Torr

Figure 9 shows the I–V characteristics of nanostructured ZnO UV sensor under UV illumination for background oxygen pressure of 7.6×10^2, 4×10^{-1}, and 8×10^{-2} Torr. Table 1 summarizes the current values for dark and UV-illuminated conditions. When the oxygen content surrounding the ZnO nanostructures was reduced, the amount of chemisorbed oxygen decreases. It was also observed that at higher oxygen pressures, the resistance is high due to saturation giving rise to lower currents [28]. Because the chemisorbed oxygen is in equilibrium with the background oxygen, there are photocurrent saturation

Table 1 Dark, photocurrent and their ratios as a function of background oxygen pressure

O_2 Pressure (Torr)	I_{Dark} (A)	I_{UV} (A)	I_{UV}/I_{Dark}
7.6×10^2	1.5×10^{-8}	1.3×10^{-7}	8.6
4×10^{-1}	1.0×10^{-7}	8.2×10^{-7}	8.2
8×10^{-2}	8.2×10^{-8}	2.8×10^{-6}	34

effects which are dominant at room conditions. However, the saturation effects depend on the geometrical shapes (like spheres in network nanowires) of nanostructures. The photoresponse plots in the range of 250–900 nm are shown in Fig. 10 for background oxygen pressures of 7.6×10^2, 4×10^{-1}, and 8×10^{-2} Torr. At higher oxygen pressure (7.6×10^2 Torr), the photoresponse signal gives a peak at 397 nm and gradually drops to zero at 310 nm. The onset of photoresponse occurs at 410 nm with a sharp peak at 397 nm and a broad peak at 367 nm. These peaks are deconvoluted using Gaussian distribution functions and correspond to the excitonic and band edge peaks in ZnO. The photoresponse plot for the background oxygen pressure of 7.6×10^2 Torr has a blind response for the incident light in the visible region. However, as the background oxygen pressure reduces, the photoresponse signal starts

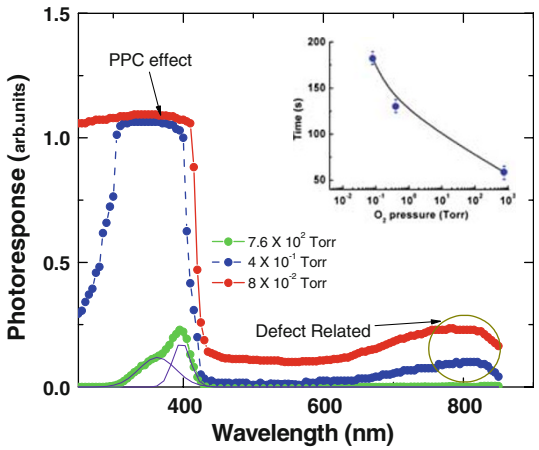

Fig. 10 Photoresponse plots for nanostructure ZnO UV sensor for 7.6×10^2 Torr and vacuum levels of 4×10^{-2} and 8×10^{-2} Torr. Note the PPC trend when the oxygen pressure is reduced. *Inset* photocurrent decay time with O_2 pressure

responding at unusually higher wavelengths between 780 and 800 nm. The mere indication of a weak response in the visible region provides some insight into evolution of defects. When the incident photon energy reaches the UV region, the main peak at 397 nm plateaus and never fades to zero even after the removal of UV incident light. This effect of photoresponse saturation in the absence of excitation leads to persistent photoconductivity, PPC. The lack of decay of the photoresponse with time is called as PPC. The inset of Fig. 10 provides the decay time of photocurrent when the UV excitation is turned off. The photocurrent decay time at 7.6×10^2 Torr was measured to be 58.5 s and is found to increase to 130 s and 182 s for background O_2 pressures of 4×10^{-1} and 8×10^{-2} Torr, respectively. Similar results have been reported by Jun et al. [29], where the authors have studied the decay time of ZnO-nanostructured UV sensor at room conditions and at reduced pressures and have observed slower decay time as the pressure was reduced due to re-adsorption of oxidizing gas molecules.

The inverse correlation between the background oxygen pressure and the photocurrent decay time clearly demonstrates the effect of oxygen on the sensor performance. PPC is commonly attributed to the existence of defects, which are metastable between shallow and deep levels and dislocations in the materials. One such defect is the deep unknown center (DX, discussed in the following section), which forms when shallow donors convert into deep donors after a large lattice relaxation [30]. When the background oxygen is depleted (4×10^{-1} and 8×10^{-2} Torr conditions), the ZnO lattice undergoes a dynamic equilibrium between the chemisorbed oxygen and the interstitial oxygen (anion) vacancies. Under these circumstances, the interstitial vacancies dominate the conduction process over the chemisorbed oxygen. The space charge regions then modulate the effective conduction cross-section of the device [31].

In an interesting paper, Lany et al. [32] have shown using first-principal electronic structure calculations that the anion vacancies in II–VI semiconductors as a class of intrinsic defects exhibiting metastable behavior and have predicted that PPC is caused by the oxygen vacancy V_O in ZnO, originating from a metastable shallow donor state. In ZnO, the anion vacancy, V_O, undergoes transformation from relaxed neutral V_O^0 to the charged oxygen vacancy V_O^{2+} (charged state) between the defect-localized states (DLS) situated within the gap, below and above the conduction band minimum (CBM), termed by the authors as "α and β type behavior", respectively. The origin of these states lies in the interaction of impurity atomic orbitals (constructed from the combinations of the dangling bonds [33]) with the states of ideal vacancy. The DLS below CBM (α type) with localized wavefunctions do not contribute to conductivity, though occupied by electrons and weakly respond to external perturbations such as pressure and temperature. The DLS above the CBM (β type) are resonant with the conduction band, and electrons will drop to the CBM to occupy a perturbed host state (PHS). The energy of the vacant orbitals depends strongly on atomic relaxation of neighboring cations. The energy state of V_O^0 is widened by inward relaxation of nearest-neighbor Zn atoms toward the vacancy site resulting in an average Zn–Zn inter atomic distance of 3 Å, whereas while forming V_O^{2+}, the Zn neighbor atoms relax outward leading to a configuration with larger Zn–Zn inter-atomic distance of 4 Å. The transition from V_O^0 to V_O^{2+} state involves intermediate steps as shown below;

$$V_O^0 \rightarrow V_O^+ + e\ldots(d_{Zn-Zn}) \approx 3\,\text{Å}$$

$$V_O^+ \rightarrow V_O^{2+} + e\ldots(d_{Zn-Zn}) \approx 4\,\text{Å}$$

When the Zn–Zn inter-atomic distance is modified by inward and outward movement, Zn vacancies (V_{Zn}) are produced which are intrinsic acceptors. The appearance of a level at $\sim$1.5 eV verifies the evolution of V_{Zn} when the background oxygen is reduced [34]. The reaction kinetics of V_O^0 thus results in metastable configuration change, constituting the PPC in ZnO. The above explanation follows very well in the present investigation of PPC phenomenon observed under depleted oxygen conditions.

To conclude, the phenomenon of PPC is a defect-related issue that depends entirely on the oxygen atmosphere around a nano-ZnO device. There has been a major thrust in fabricating nanostructured ZnO devices for gas, piezo, light, and biosensor applications. Mostly, these applications require device to be a resistor type that is prone to change by virtue of ambient rather than the stimulants, thereby opening many research opportunities to passivate the device effectively. The technique and the approach described in this paper can be extended to observe similar effects prevalent in any bulk material systems.

Acknowledgments Authors SSH and NVH acknowledge the constant support from Buck Sharpton, Vice Chancellor (Research), Daniel White, Director, Institute of Northern Engineering and acknowledge the financial support from the U.S. Defense Micro Electronic Activity (DMEA) and the U.S. Defense Advanced Research Projects Agency (DARPA) at University of Alaska, Fairbanks.

References

1. Y. Xia, P. Yang, Y. Sun, Y. Wu, B. Mayers, B. Gates, Y. Yin, F. Kim, H. Yan, Adv. Mater. **15**, 353 (2003)
2. D. Appell, Nature **419**, 553 (2002)
3. R. Grace, The 2006 report card on the barriers to the commercialization of MEMS and nanotechnology, http://www.rgrace.com/Papers/2006_Report_Card.pdf and www.rgrace.com

4. S. Nakamura, G. Fasol, *The Blue Laser Diode* (Springer, Berlin, 1997)
5. S.J. Pearton, D.P. Norton, K. Ip, Y.W. Heo, T. Steiner, Prog. Mater. Sci. **50**, 293 (2005)
6. A. Tsukazaki, A. Ohtomo, T. Onuma, M. Ohtani, T. Makino, M. Sumiya, K. Ohtani, S.F. Chichibu, S. Fuke, Y. Segawa, H. Ohno, H. Koinuma, M. Kawasaki et al., Nat. Mater. **4**, 42 (2005)
7. G. Goncalves, J. Non-Cryst. Solids **352**, 1444 (2006)
8. http://www.mda.mil/mdalink/pdf/materials.pdf
9. X.D. Wang, Y. Ding, C.J. Summers, Z.L. Wang, J. Phys. Chem. B **108**, 8773 (2004)
10. H. Kind, H. Yan, B. Messer, M. Law, P. Yang, Adv.Mater. **14**, 158 (2002)
11. C. Soci, A. Zhang, B. Xiang, S.A. Dayeh, D.P.R. Aplin, J. Park, X.Y. Bao, Y.H. Lo, D. Wang, Nano Lett. **7**, 1003 (2007)
12. Z.L. Wang, Adv. Mater. **15**, 432 (2003)
13. M.H. Huang, S. Mao, H. Feick, H. Yan, Y. Wu, H. Kind, E. Weber, R. Russo, P. Yang, Science **292**, 1897 (2001)
14. N.I. Kovtyukhova, T.E. Mallouk, Chem. Eur. J. **8**, 4354 (2002)
15. J.Z. Li, J.Y. Lin, H.X. Jiang, A. Salvador, A. Botchkarev, H. Morkoc, Appl. Phys. Lett. **69**, 1474 (1996)
16. V.V. Ursaki, I.M. Tiginyanu, P.C. Ricci, A. Anedda, S. Hubbard, D. Pavlidis, J. Appl. Phys. **94**, 3875 (2003)
17. J.Z. Li, J.Y. Lin, H.X. Jiang, M.A. Khan, Q. Chen, J. Vac. Sci. Technol. B **15**, 1117 (1997)
18. B. Claflin, D.C. Look, S.J. Park, G. Cantwell, J. Cryst. Growth **287**, 16 (2006)
19. XRD Data, Card Number 36-1451
20. C.D. Wagner, W.M. Riggs, L.E. Davis, J.F. Moulder, G.E. Mullenberg, *Handbook of X-Ray Photoelectron Spectroscopy* (Perkin-Elmer Corporation, Eden Prairie, 1979)
21. U. Ozgur, Y.I. Alivov, C. Liu, A. Teke, M.A. Reshchikov, S. Dogan, V. Avrutin, S.J. Cho, H. Morkoc, J. Appl. Phys. **98**, 041301 (2005)
22. B.S. Zou, R.B. Liu, F.F. Wang, A.L. Pan, L. Cao, Z.L. Wang, J. Phys. Chem. B **110**, 12865 (2006)
23. W. Yang, S.S. Hullavarad, B. Nagaraj, I. Takeuchi, R.P. Sharma, T. Venkatesan, R.D. Vispute, H. Shen, Appl. Phys. Lett. **82**, 3424 (2003)
24. X.G. Zheng, Q.S. Li, J.P. Zhao, D. Chen, B. Zhao, Y.J. Yang, L.C. Zhang, Appl. Surf. Sci. **253**, 2264 (2006)
25. L.J. Mandalapu, Z.F. Yang, X. Xiu, D.T. Zhao, J.L. Liu, Appl. Phys. Lett. **88**, 092103 (2006)
26. R.J. Collins, D.G. Thomas, Phys. Rev. **112**, 388 (1958)
27. D.A. Melnick, J. Chem. Phys. **26**, 1136 (1957)
28. Q.H. Li, Q. Wan, Y.X. Liang, T.H. Wang, Appl. Phys. Lett. **84**, 4556 (2004)
29. J.H. Jun, H. Seong, K. Cho, B. Moon, S. Kim, Ceram. Int. **35**, 2797 (2009)
30. D.J. Chadi, K.J. Chang, Phys. Rev. Lett. **61**, 873 (1988)
31. J.A. Garrido, E. Monroy, I. Izpura, E. Munoz, Semicond. Sci. Technol. **13**, 563 (1998)
32. S. Lany, A. Zunger, Phys. Rev. B **72**, 035215 (2005)
33. S. Lany, A. Zunger, Phys. Rev. Lett. **93**, 156404 (2004)
34. A.F. Kohan, G. Ceder, D. Morgan, C.G. Van de Walle, Phys. Rev. B **61**, 15019 (2000)